Uniaxial stress study of spin and charge stripes in La1.875Ba0.125CuO4 by 139La NMR and 63Cu NQR

Jakovac, Ivan; Dioguardi, A. P.; Grbić, Mihael Srđan; Gu, G. D.; Tranquada, J. M.; Hicks, C. W.; Požek, Miroslav; Grafe, H.-J.

Source / Izvornik: Physical Review B, 2023, 108

Journal article, Published version Rad u časopisu, Objavljena verzija rada (izdavačev PDF)

https://doi.org/10.1103/PhysRevB.108.205113

Permanent link / Trajna poveznica: https://urn.nsk.hr/um:nbn:hr:217:867795

Rights / Prava: In copyright/Zaštićeno autorskim pravom.

Download date / Datum preuzimanja: 2025-03-23



Repository / Repozitorij:

Repository of the Faculty of Science - University of Zagreb



Uniaxial stress study of spin and charge stripes in La_{1.875}Ba_{0.125}CuO₄ by ¹³⁹La NMR and ⁶³Cu NQR

I. Jakovac , ¹ A. P. Dioguardi, ^{2,*} M. S. Grbić , ^{1,†} G. D. Gu , ³ J. M. Tranquada , ³ C. W. Hicks , ^{4,5} M. Požek , ¹ and H.-J. Grafe

¹Department of Physics, Faculty of Science, University of Zagreb, Bijenička 32, Zagreb HR 10000, Croatia
²Leibniz Institute for Solid State and Materials Research, Helmholtzstrasse 20, D-01069 Dresden, Germany
³Condensed Matter Physics and Materials Science Department, Brookhaven National Laboratory, Upton, New York 11973, USA
⁴School of Physics and Astronomy, University of Birmingham, Birmingham B15 2TT, United Kingdom
⁵Max Planck Institute for Chemical Physics of Solids, 01187 Dresden, Germany

(Received 7 March 2023; revised 22 September 2023; accepted 16 October 2023; published 8 November 2023)

We study the response of spin and charge order in single crystals of La_{1.875}Ba_{0.125}CuO₄ to uniaxial stress through ¹³⁹La nuclear magnetic resonance and ⁶³Cu nuclear quadrupole resonance, respectively. In unstressed La_{1.875}Ba_{0.125}CuO₄, the low-temperature tetragonal structure sets in below $T_{\rm LTT} = 57$ K, while the charge order and the spin order transition temperatures are $T_{\rm CO} = 54$ K and $T_{\rm SO} = 37$ K, respectively. We find that uniaxial stress along the [110] lattice direction strongly suppresses $T_{\rm CO}$ and $T_{\rm SO}$, but has little effect on $T_{\rm LTT}$. In other words, under stress along [110] a large splitting (\approx 21 K) opens between $T_{\rm CO}$ and $T_{\rm LTT}$, showing that these transitions are not tightly linked. On the other hand, stress along [100] causes a slight suppression of $T_{\rm LTT}$ but has essentially no effect on $T_{\rm CO}$ and $T_{\rm SO}$. Magnetic field $T_{\rm H}$ along [110] stabilizes the spin order: the suppression of $T_{\rm SO}$ under stress along [110] is slower under $T_{\rm H}$ [110] than $T_{\rm H}$ [1001]. We develop a Landau free-energy model, and we interpret our findings as an interplay of symmetry-breaking terms driven by the orientation of spins.

DOI: 10.1103/PhysRevB.108.205113

I. INTRODUCTION

One of the leading open questions in the research of high-temperature superconductors is the relation between competing electronic orders. Even though stripe charge order (CO) is ubiquitous in cuprates, the relationship between static charge and spin order (SO) remains incompletely understood. This is partly due to the limited number of systems in which both can be studied. The other reason is that the structural, electronic, and magnetic degrees of freedom are intertwined in these orders. In La_{2-x}Ba_xCuO₄ (LBCO) close to x = 1/8 doping, CO becomes pinned as the symmetry of the lattice changes from low-temperature orthogonal (LTO) to low-temperature tetragonal (LTT) at $T_{LTT} = 57 \text{ K}$. At this doping, the CO sets in below $T_{\rm CO} \approx 54 \, \rm K$, and SO transition temperature T_{SO} reaches its maximum value [1–4] of $pprox 40\,\mathrm{K}.$ In contrast, the bulk superconducting transition temperature (T_c) is strongly suppressed. T_c rapidly increases for doping away from 1/8, even though the structural transition and CO/SO persist. It was initially hypothesized that the structural symmetry of the LTT phase is necessary for CO/SO to condense. However, Hücker et al. [5] have shown in La_{1.875}Ba_{0.125}CuO₄ under hydrostatic pressure that CO/SO appear even when long-range LTT structural order was suppressed, which softened the structural symmetry restriction. Follow-up studies found that CO was persisting in the presence of *local* LTT lattice deformations

[6,7], which put the role of structural symmetry in this compound in focus again. A similarly ambiguous connection of stripe order to the structure is also seen in other rare-earth doped systems ($\text{La}_{2-x-y}R_y\text{Sr}_x\text{CuO}_4$, R=Eu, Nd), where CO is known to appear within the LTT phase or at least close to T_{LTT} [4–12]. A complex interplay of disorder, symmetry, and electron correlations completely changes how CO/SO appears.

In this paper, we use nuclear magnetic resonance and nuclear quadrupolar resonance (NMR/NQR) to systematically study the phase diagrams of SO, CO, and LTT structure onset in the archetypal stripe compound La_{1.875}Ba_{0.125}CuO₄, controlled by in-plane uniaxial stress (σ) in the [100] and [110] directions (see Fig. 1). It has previously been reported with μ SR that stress approximately along [110] rapidly suppresses T_{SO} in La_{1.895}Ba_{0.115}CuO₄. Here, we find that $T_{\rm SO}$ is also strongly suppressed by stress along [110] in La_{1.875}Ba_{0.125}CuO₄ although the SO is more robust than for x = 0.115: larger stress is required. As magnetic field (H) is required to carry out the NMR measurements, we find that T_{SO} is suppressed more slowly for $H \parallel [110]$ than $H \parallel [001]$, pointing to a nontrivial interplay of spin direction and lattice symmetry. The CO shows the equivalent response to external stress, and the onset temperature $T_{\rm CO}$ is strongly suppressed by $\sigma_{[110]}$. However, T_{LTT} shows only a mild response to applied stress. As a result, $\sigma_{[110]}$ causes T_{CO} to separate from $T_{\rm LTT}$, with $T_{\rm LTT} - T_{\rm CO} \approx 21\,{\rm K}$ at maximal induced strain. This unexpected result resolves how structural symmetry affects the formation of stripe order in cuprates. We discuss

^{*}Present address: Los Alamos National Laboratory, Los Alamos, New Mexico 87545, USA.

[†]Corresponding author: mgrbic@phy.hr

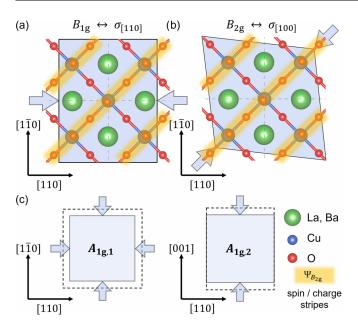


FIG. 1. Schematic of characteristic in-plane symmetry-breaking strains (a) B_{1g} (orthorhombic) and (b) B_{2g} (rhombic), and (c) symmetric, $A_{1g,1}$ and $A_{1g,2}$. The unstrained lattice in the foreground illustrates how the strain is applied with respect to the CO and SO parameter $\Psi_{B_{2g}}$, structural symmetry-breaking order parameter $\Phi_{B_{2g}}$ (octahedral tilts). B_{1g} and B_{2g} denote the irreducible representations of D_{4h} point group. Strain directions are expressed in the principal axes of the HTT phase (see the text).

these findings as an interplay of symmetry-defined terms in a self-developed Landau free-energy model that simultaneously shows a good agreement with earlier data dependence of $T_{\rm CO,SO}$ to hydrostatic pressure.

The paper is organized as follows: in Sec. II, we explain the experimental methods used in the study; in Sec. III, we present the results of La NMR and Cu NQR; in Sec. IV, we present the Landau free-energy model developed to analyze our results; in Sec. V, we discuss our findings; and we summarize in Sec. VI.

II. EXPERIMENTAL METHODS

The La_{1.875}Ba_{0.125}CuO₄ single-crystal samples were grown with the traveling solvent floating-zone method described in Ref. [13]. Samples were first properly aligned by Laue scattering and cut along the specific crystallographic directions in the high-temperature tetragonal (HTT) phase. The typical sample size used in the experiment was $4 \times 1 \times 0.5$ mm³, where the longest dimension was either [100] or [110], and the shortest was along [001]. By [110], we denote the direction along the diagonal of the CuO2 square lattice with Cu in the corners, and by [100] the direction along the Cu-O bond [see Figs. 1(a) and 1(b)]. When a symmetry-breaking stress is exerted on the sample, neither phase remains strictly orthorhombic (above T_{LTT}) nor tetragonal (below $T_{\rm LTT}$). However, we will continue using the same notation to prevent potential confusion and to stay consistent with the notation used in other articles on the topic. We characterized both samples by SQUID magnetometry in low magnetic fields of 20 Oe. They showed the same behavior below 40 K and a bulk T_c of about 5.5 K as in Ref. [14].

NMR data on lanthanum (spin I = 7/2, $\gamma_n/2\pi = 6.0146$ MHz/T) were collected on a central $(+1/2 \leftrightarrow -1/2)$ transition of the ¹³⁹La spectra using a Tecmag spectrometer with a Hahn echo pulse sequence $\pi/2 - \tau - \pi$. Typical $\pi/2$ pulse length was 0.5 µs and $\tau = 17$ µs, while pulse power was 0.5 W. With a magnetic field of 7 T, the spin-lattice relaxation rates T_1^{-1} were measured at frequency $\omega_L = 42.18 \, \mathrm{MHz}$. T_1^{-1} relaxation rates were determined by a saturation-pulse recovery sequence, after which the data were fit to a relaxation curve [15,16] for I = 7/2: $f(t) = (1/84)e^{-(t/T_1)^s} + (3/44)e^{-(6t/T_1)^s} + (75/364)e^{-(15t/T_1)^s} + (1225/1716)e^{-(28t/T_1)^s}$. The phenomenological stretching exponent s gives insight into the distribution of the relaxation times T_1 . The $s \ge 0.5$ implies the Gaussian T_1 distribution on a logarithmic scale with full width at half-maximum (FWHM) across an order of magnitude and $T_1 \approx T_{1,\text{median}}$. When s < 0.5, the distribution widens drastically, and the fitted T_1 no longer represents the distribution median [17]. NQR data on ⁶³Cu were collected on the high-frequency signal (the so-called B-line) from Cu sites near the dopant Ba ions [18]. Since in La_{1.875}Ba_{0.125}CuO₄ the B-line is well separated from the low-frequency A-line, it can be analyzed directly without additional spectral deconvolution. To acquire the signal, we employed the method reported in a previous work [19], using a Hahn echo with a typical $\pi/2$ pulse length of 0.7 μ s and $\tau = 4 \mu$ s. Since the Cu NQR line intensity rapidly diminishes [20-24] at the onset of CO, this was utilized to determine $T_{\rm CO}$.

To induce strain, we employed a uniaxial strain cell described in [25] (partly shown in Fig. 7). The applied stress was varied by applying voltages $V=\pm 200\,\mathrm{V}$, with which we were able to induce a strain up to $\varepsilon\approx 1\%$, depending on the sample orientation and dimensions. To deduce the applied stress $[\sigma\ (\mathrm{GPa})]$ from the measured strain $[\varepsilon\ (\%)]$, we used the cuprate elasticity data from [26]. Technical details are shown in Appendix A.

III. RESULTS

In Figs. 2(a) and 2(c) we present the measured temperature dependence of the spin-lattice relaxation rate T_1^{-1} for stress applied along the [110] direction. ε_{110} denotes the induced strain along the [110] direction, obtained under σ_{110} . Poisson's-ratio expansion in the transverse directions is implied. The magnetic field of 7 T was oriented along the crystal [001] axis. In the unstrained sample, T_1^{-1} starts to increase below 55 K as CO sets in. With cooling, a critical slowing down of spin fluctuations causes T_1^{-1} to increase by three orders of magnitude before reaching a maximum value at T_{SO} = 37 K at zero strain. With further cooling, T_1^{-1} slowly decreases as the fluctuations of the SO continue to slow down. For $H \parallel c$, such a temperature dependence of ¹³⁹La T_1^{-1} has been shown [23,27,28] to deviate from the Bloembergen-Pound-Purcell (BPP) mechanism [29]: $T_1^{-1}(T) = \gamma^2 h_0^2 \tau_c(T) / [1 + \frac{1}{2} T_0]$ $\omega_L^2 \tau_c^2(T)$], where h_0 is the local field fluctuating at the nuclear site, γ is the gyromagnetic ratio, $\omega_L = \gamma H$ is the nuclear Larmor frequency, and $\tau_c(T) = \tau_{\infty} \exp(E_a/k_B T)$ is the electron relaxation time, τ_c with an activation energy E_a . $T_1^{-1}(T)$ is somewhat better described by the extended BPP model where E_a is introduced with a normal distribution of values

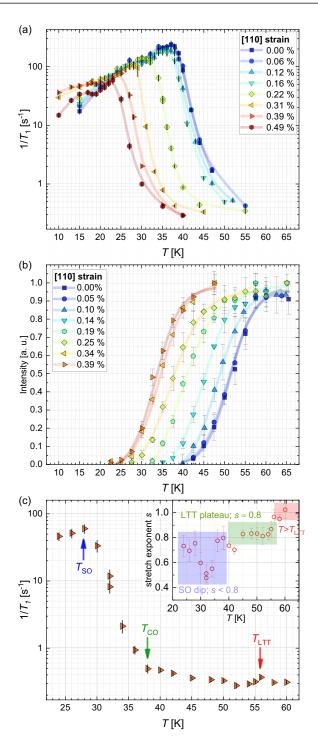


FIG. 2. (a) Temperature dependence of ^{139}La spin-lattice relaxation rate $^{139}T_1^{-1}$ for $H \parallel [001]$ and stress applied in [110]. Maximum in T_1^{-1} coincides with T_{SO} . Lines are guides to the eyes. (b) Normalized intensity of ^{63}Cu B-line measured by NQR under $\varepsilon_{[110]}$ strain. The lines are fitted to a phenomenological function I(T) (see the text). (c) T_1^{-1} measurement at uniaxial strain $\varepsilon_{[110]} = 0.4\%$ in a wide temperature range shows an anomaly at $T_{\text{LTT}} \approx 56\,\text{K}$. In the inset, stretch exponent s drops slightly at T_{LTT} , then to s=0.5 close to T_{SO} . The legend shows the values of measured $\varepsilon_{[110]}$ and $\varepsilon_{[100]}$ strain.

of a typical width 80 K, although it still cannot account for the complete behavior. The distribution of E_a is typically explained by the intrinsic level of disorder in the cuprates.

Nevertheless, we shall discuss some aspects of the observed $T_1^{-1}(T)$ dependence (however, only qualitatively) through BPP model parameters since despite its limitations, no better model is currently available.

When stress is applied along [110], for measured $\varepsilon_{[110]}$ strain values larger than 0.1% (\approx 180 MPa), $T_{\rm SO}$ shifts to lower temperatures. Also, the peak value of T_1^{-1} at T_{SO} decreases. The width of the SO transition does not broaden, even at the highest stress value where T_{SO} is reduced by more than 35%, indicating a high level of strain homogeneity, and no increase of the E_a values distribution as the sample is compressed. For temperatures below T_{SO} , we see that the relaxation values under stress are not simply shifted like those for $T > T_{SO}$, but that the values smoothly connect to the $T_1^{-1}(T)$ dependence measured at zero stress, so that $T_1^{-1}(T, \varepsilon_{[110]})$ remain practically unchanged down to 20 K. Within the BPP model, this would indicate that the electronic fluctuation time τ_c is unaffected (or reduces together with h_0) by stress, and is determined by the absolute temperature value T rather than $T - T_{SO}$. This is not what is typically observed with the suppression of a magnetic transition by doping or strain. One would expect that (e.g., see Fig. 3 in [30] or Fig. 6 in [31]) as $\sigma_{[110]}$ destabilizes SO, an increase in spin fluctuations would increase T_1^{-1} for $T \leq T_{SO}$. Current behavior indicates a complex relationship between H and fluctuations of stripe SO.

To characterize the response of CO to $\varepsilon_{[110]}$, we measured the temperature dependence of the integrated intensity of the high-frequency copper NQR signal (B-line) in the vicinity of $T_{\rm CO}$, shown in Fig. 2(b). It has been well established that the intensity of the B-line I(T) reduces with the onset of CO due to the effect known as wipeout [20-24]. Recently, it was shown that the wipeout in La_{1.875}Ba_{0.125}CuO₄ is caused by incoherent spin fluctuations and the increase of NQR linewidth [19]. To analyze our data systematically, every measured I(T)dependence was corrected for temperature and then fitted to a simple phenomenological function $(\tanh ((T - T_h)/w) +$ 1)/2, where T_h is the mid-transition temperature and w is the width of the transition. Clearly, T_h is related to CO onset temperature as $T_{CO} = CT_h$, where the constant C = 1.055 is set by the $T_{\rm CO}$ value at zero strain ($T_{\rm CO}=54\,{\rm K}$). The value of C was kept the same for all strains as the width w and the shape of the transition do not change with strain. Figure 2(b) shows that the T_{CO} is strongly suppressed by $\varepsilon_{[110]}$.

When the applied stress is sufficient to separate $T_{\rm SO}$ and $T_{\rm CO}$ from $T_{\rm LTT}$, one can observe all the characteristic temperatures in $T_1^{-1}(T)$ measurements alone. For example, in Fig. 2(c) we show $T_1^{-1}(T)$ dependence in a wide temperature range at $\varepsilon_{[110]}=0.4\%$ where $T_{\rm SO}$ and $T_{\rm CO}$ are easily noticeable. The small peak structure close to 56 K is attributed to $T_{\rm LTT}$, which we have determined independently, and we will discuss it later in the text. This measurement of $T_1^{-1}(T)$ was done on a different sample of the same doping, and as we can see the characteristic temperatures match those determined previously, which shows a high degree of reproducibility.

The behavior of T_1^{-1} under $\sigma_{[110]}$ is in stark contrast to that set by stress along [100] ($\sigma_{[100]}$) shown in Fig. 3. Here, $T_1^{-1}(T)$ is essentially unaffected, even at the highest stress values. Hence, T_{SO} does not change with $\varepsilon_{[100]}$. From the inset of the figure we can see that this strain direction does not affect T_{CO} , either.

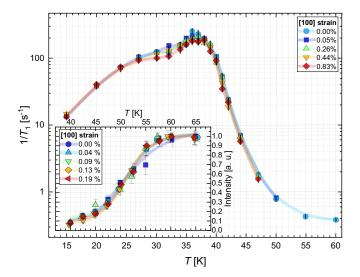


FIG. 3. Temperature dependence of $^{139}T_1^{-1}$ measured with stress applied along [100] and $H \parallel$ [001]. Lines are guides to the eyes. The inset shows the NQR measurements of copper B-line at $\sigma_{[100]}$. Lines are fits to the phenomenological function I(T) (see the text). The legend shows the values of induced strain.

With T_1^{-1} , we also measured the spectral features of the 139 La central transition (shown in Appendix B) which showed no anomalous change in linewidth or shape with temperature and stress in the region of our measurements. Hence, we conclude that samples have only undergone elastic deformation without reaching a plastic regime or cracking. Furthermore, the distribution of T_1 times, characterized by the stretching exponent s of the relaxation curves, shows the characteristic behavior observed in earlier studies [28].

The suppression of $T_{\rm SO}$ by $\epsilon_{\rm [110]}$ is similar to that reported by $\mu \rm SR$ on an x=0.115 doped sample for stress along a specific direction aligned at an angle of 30° relative to the Cu-O bond [32]. There, the authors reported a drop of $T_{\rm SO}$ values down to 30 K for $\sigma \approx 40$ MPa, after which it reached a saturated value that barely changes up to the highest stress value of 90 MPa. However, at 1/8 doping the SO is more robust [3,4,33], and this is why larger stress is needed to equally suppress $T_{\rm SO}$. Our results reveal that the major effect

of SO suppression actually comes from stress along [110] direction.

To check how stress influences the LTO-LTT transition, we combined the measurements of $T_1^{-1}(T)$ and the data of voltage and capacitance measured at the strain cell. By lowering the temperature across T_{LTT} , a clear anomaly is seen in displacement (see Fig. 11 in Appendix C), caused by the change in compressibility across the structural transition [26]. The anomaly is small enough not to influence the overall value of applied stress but remains within the resolution of our measurement setup. As mentioned earlier, the $T_{\rm LTT}(\varepsilon)$ dependence is also confirmed by measurements of T_1^{-1} , which shows a small peak at $T_{\rm LTT}$. Similar behavior has been observed [28] at the HTT/LTO structural transition, and at the LTO/LTT transition in La_{1.65}Eu_{0.2}Sr_{0.15}CuO₄ [9]. We found no noticeable effect on the onset of the LTT phase with stress applied along [110], as is shown in Fig. 4(a). However, stress along the [100] direction causes a slow but definite suppression of $T_{\rm LTT}$. This is qualitatively similar to what was observed [10] in La_{1.475}Nd_{0.4}Sr_{0.125}CuO₄, albeit of smaller size, since there $\varepsilon_{[100]}$ strain of \approx 0.046% reduced $T_{\rm LTT}$ from 63 to 34 K. A reason could be that the system is close [8,34,35] to a triple structural transition point rendering T_{LTT} more susceptible to external stress.

From these results, we generate the (in-plane)-stress controlled phase diagrams depicted in Fig. 4. To the best of our knowledge, this is the first time that one has traced the behavior of all three temperatures under stress. For stress $\varepsilon_{[110]}$ above $\approx 0.06\%$, $T_{\rm CO}$ separates from $T_{\rm LTT}$, and $T_{\rm LTT}-T_{\rm CO}$ reaches 21 K at maximum strain—a dramatic change in the behavior reminiscent of the situation in La_{1.8-x}Eu_{0.2}Sr_xCuO₄ where $T_{\rm LTT}\approx 130\,{\rm K}$ and $T_{\rm CO}$ reaches 80 K at x=0.125 doping [36]. Up to this point, it was not possible to achieve a similarly large difference between $T_{\rm LTT}$ and $T_{\rm CO}$ in another system at 0.125 doping. These data show that one can indeed separate them by inducing the strain of a specific direction.

Looking back on T_1^{-1} data in Fig. 2(a), in an earlier study [28] it was found that ¹³⁹La T_1^{-1} shows a magnetic-field-induced anisotropy connected to the relative orientation of spins [37] in the SO stripes with respect to the external magnetic field. In particular, in the SO state, T_1^{-1} is approximately an order of magnitude larger for $H \parallel [001]$ in comparison to

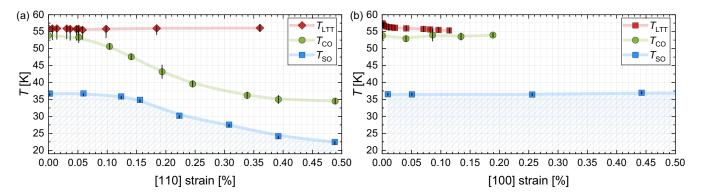


FIG. 4. Strain-temperature phase diagram for $H \parallel c$ and stress applied (a) along the [110] direction, and (b) along the [100] direction. The data points are extracted from the data of Figs. 2 and 3 and show that $\sigma_{[110]}$ reduces T_{SO} (blue) and T_{CO} (green), even though the onset of LTT structural phase remains the same (red). However, $\sigma_{[100]}$ does not change T_{SO} at all, while T_{LTT} shows a mild drop. Lines are guides to the eyes.

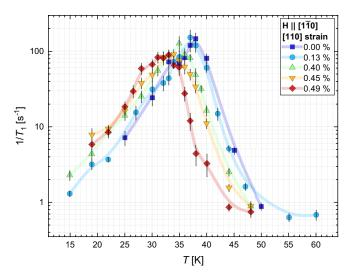


FIG. 5. Temperature dependence of $^{139}T_1^{-1}$ measured with stress $\sigma_{[110]}$ and $H \parallel [1\overline{1}0]$. Lines are guides to the eyes. The suppression of $T_{\rm SO}$ is greatly reduced. The legend shows the values of measured strain.

 $H \parallel [110]$ (or $[1\overline{1}0]$). This difference is not caused by the anisotropic hyperfine coupling since it would then be visible even in the paramagnetic state, but rather the anisotropy reflects the property of the SO state. As was mentioned earlier, the lack of increase of T_1^{-1} below T_{SO} in Fig. 2(a) also shows an unusual relationship between spin fluctuations and magnetic field. To further clarify the nature of this anisotropy, we applied stress again along the [110] direction, but this time with $H \parallel [1\overline{1}0]$. The results are shown in Fig. 5: for the unstressed sample, we reproduce the T_1^{-1} values within the SO phase from [28]. What is surprising, though, is that reorientation of the magnetic field drastically reduces the stress-driven suppression of T_{SO} . With $H \parallel [110]$, T_{SO} is reduced to only 32 K (which is $\Delta T \approx 5$ K from zero-stress value) at a [110] strain of 0.49% (\approx 0.9 GPa). This change in T_{SO} corresponds to an overall rate of 10.2 K/% (\approx 5.63 K/GPa), which is significantly less than 27.5 K/% (\approx 15.2 K/GPa) obtained for $H \parallel [001]$. Clearly, the magnetic field along $[1\overline{1}0]$ reduces the effect of stress and acts as a stabilizing factor to stripe SO. This surprising result, seemingly unique to LBCO, has been implied previously [28,37], but in this study it is directly revealed.

Another observation can be made from Fig. 5 for $\varepsilon_{[110]} > 0.13\%$: in addition to the gradual shifting of $T_{\rm SO}$ to lower temperatures, it can be seen that the T_1^{-1} values (i.e., spin fluctuations) increase for $T < T_{\rm SO}$, as is expected for suppressed magnetic order. Hence, spin fluctuations now seem to depend on $T - T_{\rm SO}$. This would indicate that the unusual anisotropy of the SO fluctuations persists even under stress.

We have not explored how magnetic field influences CO, since NQR measurements (performed in zero magnetic field) allow us to isolate the copper signal for a specific doping environment (B-line). When the magnetic field is applied, the NMR lines start to overlap, and it is no longer simple to assign changes in the spectra to a specific phenomenon of the stripe physics.

IV. FREE-ENERGY MODEL

To address the markedly different strain dependencies of the onset temperatures T_{LTT} and $T_{CO,SO}$, we consider a simple Landau free-energy (LFE) model. A similar approach has led to the development of the linear two-component orderparameter model [38] to explain the doping dependence of $T_{\rm LTT}$ in LBCO [39], the stiffness constant softening observed in ultrasound experiments [40], and the out-of-plane component of magnetic moment in certain cuprate systems [41,42]. Although such a two-component approach was prevalent, it lacked the higher-order contributions necessary to model the response to symmetry-breaking in-plane strains. Thus, the strain-related research on the iron pnictides shifted the focus to the simpler, symmetry-defined, LFE models [43–45], which helped to elucidate how the nematic order in iron pnictides couples to the symmetry-breaking strains. We can apply the same arguments to characterize the observed $T_{\text{CO.SO}}$ suppression in La_{1.875}Ba_{0.125}CuO₄.

First, we focus on the SO transition revealed by the ^{139}La T_1^{-1} data. In the LTT phase, the $\text{La}_{1.875}\text{Ba}_{0.125}\text{CuO}_4$ crystal point group is tetragonal $D_{4\text{h}}$; however, due to the octahedral tilts along $\pm [100]$ crystallographic axes, for a single CuO_2 layer, the in-plane symmetry is reduced. We model the LTT phase by introducing the structural order into the $D_{4\text{h}}$ symmetric planes. In the case of LBCO, both structural $(\Phi_{B_{2g}})$ and spin $(\Psi_{B_{2g}})$ order transform as the B_{2g} irreducible representation of the unstrained sample's point group $D_{4\text{h}}$. One can readily use the same model to describe the observed suppression of T_{CO} , since both spin and charge order possess the same symmetry.

The strain tensor components can be written as an in-plane symmetric $[\varepsilon_{A_{1g,1}} = \frac{1}{2}(\varepsilon_{xx} + \varepsilon_{yy}), \ \varepsilon_{A_{1g,2}} = \varepsilon_{zz}]$ and antisymmetric $[\varepsilon_{B_{1g}} = \frac{1}{2}(\varepsilon_{xx} - \varepsilon_{yy}), \ \varepsilon_{B_{2g}} = \varepsilon_{xy}]$ linear combination [46]. The out-of-plane shear strain components ε_{xz} and ε_{yz} , which form a two-dimensional $E_g(1,2)$ representation of the group, are absent in our measurements and will be omitted from the model. The minimal LFE model is given by

$$F = F_{\Psi} + F_{\Psi\varepsilon} + F_{\Psi\Phi} + F_{\varepsilon}, \tag{1}$$

where $F_{\Psi} = \Psi_{B_{2g}}^2 a(T - T_{\text{CO,SO}}) + \Psi_{B_{2g}}^4 b/2$ are the usual LFE terms (a, b > 0) which lead to the second-order phase transition, $F_{\Psi\varepsilon}$ and $F_{\Psi\Phi}$ are spin/charge-strain and spin/charge-structure coupling terms, respectively, and F_{ε} is the elastic energy. To the lowest order in $\Psi_{B_{2e}}$, we have

$$F_{\Psi\varepsilon} = \alpha_1 \varepsilon_{A_{1g,1}} \Psi_{B_{2g}}^2 + \alpha_2 \varepsilon_{A_{1g,2}} \Psi_{B_{2g}}^2 + \beta \varepsilon_{B_{1g}}^2 \Psi_{B_{2g}}^2 + \gamma \varepsilon_{B_{2g}} \Psi_{B_{2g}},$$
(2)

where the parameters α_1 and α_2 define the coupling strength to the symmetric strain, and β and γ to the antisymmetric strain. The symmetry considerations allow for a quadratic charge- and spin-structure coupling $F_{\Psi\Phi}^{(\text{CO},\text{SO})} = \delta \Phi_{B_{2g}}^2 \Psi_{B_{2g}}^2$, due to the difference between charge (spin) and structure order wave vectors. Finally, the elastic energy is given by

$$F_{\varepsilon} = \varepsilon_{A_{1g,1}}^{2}(C_{11} + C_{12}) + C_{33}\varepsilon_{A_{1g,2}}^{2}/2 + \varepsilon_{B_{1g}}^{2}(C_{11} - C_{12}) + 2C_{13}\varepsilon_{A_{1g,1}}\varepsilon_{A_{1g,2}} + 2C_{66}\varepsilon_{B_{2g}}^{2}.$$
 (3)

As presented, LFE also captures the evolution of CO/SO parameter magnitude $|\Psi_{B_{2g}}|$ with the changes in structural order $\Phi_{B_{2g}}$, but this should not affect the $T_{\text{CO,SO}}$. Hence, we will only focus on $T_{\text{CO,SO}}$ since we have no data to discuss the magnitude.

The emergence of CO and SO induces spontaneous strains in the lattice when cooled below $T_{\rm CO,SO}$, which form a rhombic distortion, suggesting that the external rhombic [100] stress [Fig. 1(c)] would only lead to a finite order parameter at all temperatures [46], and a crossover instead of a phase transition (see Appendix D). However, the crossover of the CO and SO transitions (detected by, e.g., temperature broadening) is not visible in our measurements in Fig. 3, so we can conclude that the coupling to the rhombic strain is minimal. On the other hand, orthorhombic strain [110] breaks an additional symmetry, introducing more terms into the electronic Hamiltonian, and it acts as a tuning parameter for the CO and SO transitions.

Minimizing the LFE in Eq. (1) with respect to the order parameter $\Psi_{B_{2g}}$ exposes a functional correlation between the applied stress and both structural and spin transition temperatures. Moreover, the intricate strain-order interaction will cause the structural strain to appear in the ordered phase without external stress (see Appendix D for more details). For clarity, we have replaced all elastic constants C_{ij} with the appropriate elasticity parameters (Young moduli and Poisson ratios).

V. DISCUSSION

We take applied stress as a control parameter to uncover the $T_{\rm CO,SO}$ dependence on the measured strain. While below the $T_{\rm CO,SO}$ the elastic constants are renormalized by the emergent order [47], above the transition temperature the strain on the sample depends only on its elastic properties. For stress along [100], the dependence of the $T_{\rm CO,SO}$ is then proportional to the symmetric stress contributions:

$$\frac{\partial T_{\text{CO,SO}}}{\partial \sigma_{\text{I1001}}} = \frac{\alpha_1 (1 - \nu_{\text{in}}) - 2\alpha_2 \nu_{\text{out}}}{2Y_{\text{I1001}} a},\tag{4}$$

where $\nu_{\rm in}$ and $\nu_{\rm out}$ are in-plane and out-of-plane Poisson ratios, respectively, and $Y_{[100]}$ is a Young modulus along the [100] axis. The lack of any observable change in the $T_{\rm SO}$ and $T_{\rm CO}$ measurements under $\sigma_{[100]}$ suggests that the two symmetric stress contributions in (4) are either small or exactly cancel each other out. In contrast, when applying [110] stress to the sample, from (2), we expect the $T_{\rm CO,SO}(\sigma)$ dependence to be quadratic:

$$T_{\text{CO,SO}}(\sigma_{[110]}) = T_{\text{CO,SO}}^{(0)} + \alpha_{\text{eff}}\sigma_{[110]} + \beta_{\text{eff}}\sigma_{[110]}^2,$$
 (5)

where $\alpha_{\rm eff} = \partial T_{\rm CO,SO}/\partial \sigma_{[100]}$ [i.e., exactly expression (4)] and $\beta_{\rm eff} = -4\beta/(G_{\rm xy}^2 a)$. $\alpha_{\rm eff}$ and $\beta_{\rm eff}$ are effective parameters from α_1 , α_2 , and β of the LFE model, with $G_{\rm xy}$ denoting the inplane shear modulus, and $T_{\rm CO,SO}^{(0)}$ is the CO (or SO) transition temperature of the unstrained sample (see Appendix D). The exact values of LFE expansion parameters α_1 , α_2 , and β for either CO or SO are determined from the effective coefficients, and from experimental data, and they rely on a precise quantification of the sample's elastic properties.

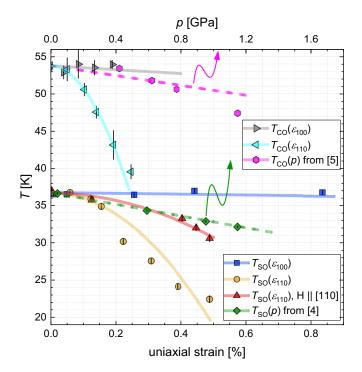


FIG. 6. $T_{\rm SO}$ and $T_{\rm CO}$ suppression induced by different strains (lower axis) and hydrostatic pressure p (top axis). The points are experimental data showing either strain dependence from this work, or hydrostatic pressure dependence from Ref. [4] (p > 1.2 GPa data are omitted for clarity) and Ref. [5]. Full thick lines mark curves fitted to the LFE model (see the text), while dashed lines are predictions of $T_{\rm CO,SO}(p)$ calculated from the model. Curvy arrows indicate hydrostatic pressure data (measured and calculated) should be read on the top axis.

Using the elasticity data from [26], we apply the LFE model to our SO measurements by fitting (4) and (5) simultaneously, and yield (shown in Fig. 6) $\alpha_{\rm eff}^{\rm SO} = -(0.3 \pm 1.0)\,{\rm K/GPa}$ and $\beta_{\rm eff}^{\rm SO} = -(21.3 \pm 4.0)\,{\rm K/GPa}^2$ for the magnetic field aligned along the c axis ([001]).

To test the validity of our model, we wish to use it to calculate the expected $T_{\rm SO}$ suppression under hydrostatic pressure (p), and we compare it to the values measured in Ref. [4]. From the model, it follows that $T_{\rm SO}(p)$ dependence is defined as

$$\frac{\partial T_{\text{SO}}}{\partial p} = \frac{\partial T_{\text{SO}}}{\partial \sigma_{[100]}} - \frac{\alpha_1 \nu_{\text{out}}}{Y_{[100]}a} + \frac{\alpha_2}{Y_{[001]}a}.$$
 (6)

The first term (i.e., $\alpha_{\rm eff}$) characterizes the reaction to the inplane symmetric stress $\varepsilon_{A_{\rm Ig,1}}$, which we previously determined to be negligible. Once elastic constants and $T_{\rm SO}(\varepsilon)$ data are inserted, we can calculate that the expected hydrostatic suppression rate of $\frac{\partial T_{\rm SO}}{\partial p} = -(3.9 \pm 2.1)\,{\rm K/GPa}$ (dashed green line in Fig. 6). This value fits nicely to the comprehensive $\mu{\rm SR}$ data set. Data for higher pressures were omitted for clarity. It should be kept in mind that the analysis is valid only until additional degrees of freedom, not accounted for in the model, start to contribute—e.g., interlayer coupling and suppression of the LTT phase with pressure.

Once the magnetic field is oriented along the [1 $\overline{10}$], it reduces the $T_{SO}(\sigma_{[110]})$ dependence drastically. From the LFE

model-based symmetry point of view, we can look at it in the following way: qualitatively, we expect the in-plane magnetic field $H_{[1\bar{1}0]}$ to act on the $\Psi_{B_{2g}}$ magnetic order by breaking an additional symmetry. Therefore, the subsequent application of the in-plane stress is no longer symmetry-breaking, so the observed suppression of the T_{SO} is diminished. Overall, the effects of the magnetic field are twofold: the increase in in-plane magnetization, which leads to a nonvanishing Zeeman contribution to the free energy, and symmetry-breaking realized by the rotation of the in-plane magnetic moments [37] through a spin-flop transition. The Zeeman contribution seems to be negligible since we do not observe a shift in T_{SO} upon field rotation from [001] to [110] at zero strain. To address the spin rotation, we utilize an atypical two-component order parameter represented just by the B_{1g} and B_{2g} antisymmetric components:

$$\begin{pmatrix} \Psi_{B_{1g}} \\ \Psi_{B_{2g}} \end{pmatrix} = \begin{pmatrix} \Psi_0 \cos(2\phi) \\ \Psi_0 \sin(2\phi) \end{pmatrix}, \tag{7}$$

where $\Psi_0(H)$ is the field-dependent order-parameter magnitude, and angle ϕ describes a continuous rotation of the magnetic moments from the [100] and [010] directions to the [110] direction. To the lowest order in Ψ , this renormalizes the quadratic suppression coefficient $\beta_{\rm eff}$ upon applying [110] strain, while the behavior seems unchanged under symmetric strains.

It would be interesting to utilize our model and reproduce data in other systems. However, this is possible only if the complete strain data (for both [100] and [110] directions) are available. At the moment, only the present work has determined $T_{SO}(\varepsilon_{[100]})$ and $T_{SO}(\varepsilon_{[110]})$ dependencies. We can note, nonetheless, that the same model holds for the hydrostatic suppression of the CO observed in Ref. [5], and thus we can repeat the analysis to predict $T_{CO}(p)$ using our $T_{CO}(\varepsilon)$ data. As we have shown in Fig. 4(b), the left-hand side of expression (4) is again negligible, which [when combined with (5)] leads to the following values of coefficients: $\alpha_{\rm eff}^{\rm CO} = -(1 \pm 5) \, {\rm K/GPa}$ and $\beta_{\rm eff}^{\rm CO} = -(85 \pm 26) \, {\rm K/GPa}^2$. The larger uncertainty here probably stems from a small number of points measured for $T_{\rm CO}(\varepsilon_{[100]})$ (the used sample was thicker than others, and thus maximum strain was limited by the maximum available stress our cell could apply). From these coefficients we calculate the expected behavior of $T_{CO}(p)$ and show it as a dashed magenta line in Fig. 6. One should note that the $T_{CO}(p)$ data from Ref. [5] have large error bars for pressure values, which lead to larger uncertainty in determined T_{CO} values, which is not shown in the figure. Nonetheless, the resulting curve follows the experimental data reasonably well.

The disappearance of CO in La_{1.8-x}Eu_{0.2}Sr_xCuO₄ has been viewed as entropy-driven [36], since LTT sets in so high that thermal energy destabilizes and melts the CO structure [24] before $T_{\rm CO}$ approaches $T_{\rm LTT}$. In La_{1.875}Ba_{0.125}CuO₄, $T_{\rm LTT}$ does not increase with strain, so if the same mechanism is at work it would mean that the LTT structure amplitude reduces with strain, which unpins the CO and thus suppresses $T_{\rm CO}$ from the zero strain value of 54 K. This reduction of LTT amplitude is indeed seen in a recent work [48] on an x = 0.115 doped sample, but it will require a separate study to check if it applies for the 1/8-doped sample.

One cannot help but wonder how stress along [001] influences SO/CO. However, as such a study has various challenges, it is a topic for future work.

VI. CONCLUSION

In summary, using ¹³⁹La NMR relaxation rate T_1^{-1} and ⁶³Cu NQR spectra, we present a complete study of the phase diagrams of stripe spin order (SO), stripe charge order (CO), and LTT structure onset in La_{1.875}Ba_{0.125}CuO₄, set by in-plane uniaxial strain (ε) in [100] and [110]. While the SO is more robust than at x=0.115 doping, for $H\parallel[001]$ $\sigma_{[110]}$ stress dramatically suppresses T_{SO} and no change is found for $\sigma_{[100]}$, which limits the applicability of theoretical models. Moreover, $H\parallel[1\bar{1}0]$ stabilizes the spin order.

CO shows the same response to strain as SO—it is suppressed by $\varepsilon_{[110]}$ alone. The suppression decouples $T_{\rm CO}$ and $T_{\rm LTT}$ temperatures for $\varepsilon_{[110]} \geqslant 0.06\%$, and at maximum strain $T_{\rm LTT} - T_{\rm CO}$ even reaches 21 K. This separation reveals the role of symmetry in connecting two seemingly different doping phase diagrams—that of ${\rm La_{2-x}Ba_xCuO_4}$ and ${\rm La_{1.8-x}Eu_{0.2}Sr_xCuO_4}$. Our results are understood using a symmetry-defined self-developed Landau free-energy model that simultaneously shows a good agreement with existing data on hydrostatic $T_{\rm SO}(p)$ and $T_{\rm CO}(p)$ dependencies.

ACKNOWLEDGMENTS

The authors acknowledge the help of Christian Blum and Dina Bieberstein in preparing the samples, Sebastian Gass for SQUID measurements, and Markus Hücker and Ivan Kupčić for valuable discussions. The work was supported by the Croatian Science Foundation (Grant No. IP-2018-01-2970), DFG (Grant No. DI2538/1-1), the Alexander von Humboldt Foundation (Grant No. 3.4-1022249-HRV-IP), and the project CeNIKS cofunded by the Croatian Government and the EU/ERDF—Competitiveness and Cohesion Operational Programme (Grant No. KK.01.1.1.02.0013). The work at BNL was supported by the U.S. Department of Energy, Office of Basic Energy Sciences, Contract No. DE-SC0012704. C.W.H. acknowledges support from DFG; TRR 288-422213477 (Project No. A10).

APPENDIX A: TECHNICAL DETAILS OF THE MEASUREMENT SETUP

In Fig. 7, we show a part of our measurement setup with the sample and an NMR coil in a strain cell. The cell operation and strain analysis are described in [25]. To gauge the uniaxial stress transferred to the sample, we used a simplified model:

$$\sigma_{\rm a} = \frac{Y_{\rm a}\Delta L}{2\lambda + l_{\rm o}},$$

where Y_a is a Young modulus along a given axis, ΔL is a measured displacement change, and l_0 is the initial size of the sample along the strained dimension. The parameter λ , defining a lengthscale over which the stress is transferred to the sample, is given by

$$\lambda = \sqrt{\frac{Y_{\rm a}td}{2G}},$$

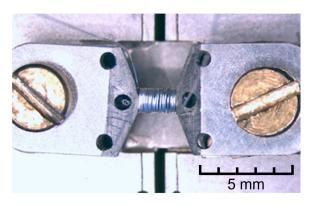


FIG. 7. NMR coil with the sample in the uniaxial cell.

where t and d denote the thickness of the sample and epoxy, respectively, and G is a shear strain modulus of the epoxy. We assume the epoxy to be an isotropic elastic material, and thus $G = Y_{\rm epoxy}/(2+2\nu)$, where we take the Young modulus and Poisson ratio to be $Y_{\rm epoxy} = 15$ GPa and $\nu = 0.3$ [49]. Unfortunately, the elastic constants for LBCO at 1/8 doping were not determined at cryogenic temperatures. However, data for similar compounds such as LSCO [26] or LCO [40] correspond to the transferred stress on the order of ≈ 1.5 GPa at the highest applied voltages. Finally, we have calculated the relative strain loss to the epoxy:

$$\eta_{\text{loss}} = \frac{\Delta L - \Delta l_{\text{sample}}}{\Delta L} = \frac{2\lambda}{2\lambda + l_0},$$

which amounts to the loss $\eta_{loss} \approx 0.4 - 0.5$ for all our samples.

APPENDIX B: NMR DATA ACQUISITION INFORMATION

1. Lanthanum spectra

In Fig. 8, we show temperature corrected ¹³⁹La NMR spectra with uniaxial strain applied along the [110] axis for a magnetic field along the [001] axis. We have observed no

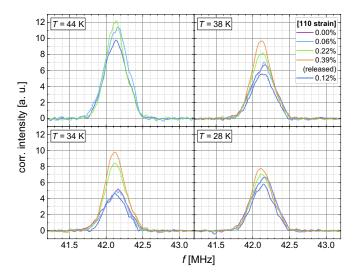


FIG. 8. 139 La NMR spectra (central transition) under different [110] uniaxial strains, at chosen temperatures above and below T_{SO} .

significant change in spectral width and frequency with the applied [100] or [110] uniaxial strain. We attribute a noticeable decrease in the signal intensity across $T_{\rm SO}$ to the enhanced longitudinal spin fluctuations near the spin-order transition. The spectra differ at intermediate temperatures due to the varying extent of the $T_{\rm SO}$ suppression with the applied [110] uniaxial strain. At low temperatures ($T < 28 \, \rm K$), when spin fluctuations under different strains become comparable [Fig. 1(a)], the line shapes coincide again. The effect is most noticeable at $T = 34 \, \rm K$. Here, at low strains, the spectrum is measured precisely, or a bit below $T_{\rm SO}$, and thus the spectral intensity is significantly diminished. The change in the signal intensity is hardly noticeable at the highest strains, but it becomes pronounced once again when the strain is released. When the strain is released, the original line shape is recovered.

2. Lanthanum relaxation curves

The fitting of spin-lattice relaxation data of 139 La central transition was done using the appropriate expression for the spin I = 7/2 [15,16]: $f(t) = (1/84)e^{-(t/T_1)^s} + (3/44)e^{-(6t/T_1)^s} + (75/364)e^{-(15t/T_1)^s} + (1225/1716)e^{-(28t/T_1)^s}$. The phenomenological stretching exponent s gives insight into the distribution of the relaxation times T_1 , as is explained in the main text. In three panels of Fig. 9, we show the relaxation data and fits for zero strain, at temperatures of 30, 41, and 60 K. The temperatures were selected to show the fit quality at three representative regimes of relaxation that have different stretch exponent values, further discussed in the next paragraph.

To accurately interpret the measured T_1 NMR relaxation data, we shall discuss the temperature and strain dependence of the fitted stretch exponent s (Fig. 10). When we approach the spin-order transition temperature $T_{\rm SO}$ for a given strain, the s dips abruptly. This behavior has already been observed in various cuprate systems, which exhibit a glassy type spin-order transition [50,51]. We can see that the spatial distribution of T_1 times broadens significantly, but the stretch exponent stays predominantly larger than the threshold value of $s \approx 0.5$. It is therefore appropriate to analyze the fitted T_1 values as they always stay within $\sim 20\%$ of the distribution median. Conversely, it is justifiable to take a fixed value of s to facilitate the interpretation of the fitted T_1 values [23].

APPENDIX C: OBSERVING THE LTO-LTT TRANSITION

Although the capacitive dilatometer of our strain cell has lower sensitivity than custom thermal-expansion measurement setups, it was sufficiently sensitive to detect a first-order LTO-LTT structural transition. We performed an exhaustive set of temperature sweeps at different uniaxial strains to characterize a change in the structural transition temperature $T_{\rm LTT}$. We used two sweep rates, $r_1 = 1~{\rm K/min}$ and $r_2 = 0.5~{\rm K/min}$, with each data set measured for both cooling and warming, while the piezo stack voltage was held constant. Therefore, the observed displacement change should only come from the thermal expansion of the strain cell or the change in the sample's elastic properties. With the former being negligible in the measured temperature range, we can easily follow a structural transition as we increase the uniaxial stress on the sample.

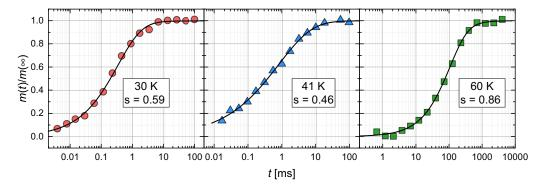


FIG. 9. Stretching exponent s fitted to our measurements. For clarity, we show only a subset of measured [110] strains with interpolated cubic splines as guides to the eye. Change in s close to the transition temperature T_{SO} is undoubtedly visible, and the strain dependence of the observed dip follows the same pattern as the T_1 data. The color-coded arrows mark T_{SO} at respective strain.

When applying [110] uniaxial stress, the change in $T_{\rm LTT}$ is absent or too small to be revealed by this method. In contrast, with the application of [100] stress, the sample displays a gradual, linear suppression of the $T_{\rm LTT}$ visible in Fig. 11. Arguably, [100] stress promotes orthorhombicity and suppresses the transition to the LTT phase.

To confirm our dilatometry measurements, we look for the LTO-LTT structural transition in our T_1 NMR measurements. Using uniaxial stress along the [110] direction, we suppress the spin transition down to $T_{\rm SO}\approx 28\,\rm K$, revealing a discernible anomaly at $T_{\rm LTT}\approx 56\,\rm K$ which roughly coincides with the LTO-LTT transition. A similar feature was already observed in LESCO [9], where the structural transition is separated from $T_{\rm SO}$ at zero strain. In addition to the slight increase in T_1^{-1} relaxation rate, there is a discernible dip in stretch exponent s [Fig. 2(c)] below $T_{\rm LTT}$, which implies a broader spatial distribution of the relaxation times T_1 . This is consistent with the mixed phase associated with the first-order structural transition.

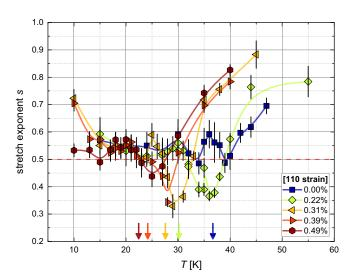


FIG. 10. Stretching exponent s fitted to our measurements. For clarity, we show only a subset of measured [110] strains with interpolated cubic splines as guides to the eye. Change in s close to the transition temperature $T_{\rm SO}$ is undoubtedly visible, and the strain dependence of the observed dip follows the same pattern as the $T_{\rm I}$ data. The color-coded arrows mark $T_{\rm SO}$ at respective strain.

APPENDIX D: CALCULATION OF THE LANDAU FREE-ENERGY MODEL

In the uniaxial strain experiment, it is advantageous to take the external stress applied on the sample as an independent variable. However, it is the induced strain that governs the suppression of the spin (charge) order transition temperature $T_{\rm CO,SO}$, so it is essential to handle the stress-strain conversion properly. In cuprates, and especially for LBCO and LSCO [26,40], the elastic constants are given along the crystallographic axes of the high-temperature (HTT) phase. Suppose we wish to construct our free-energy model in the LTT phase where the spin order sets in. In that case, we must transform the components of the stiffness matrix $\bf C$ using the familiar fourth-order tensor rotation formula:

$$C'_{ijkl} = c_i c_j c_k c_l C_{ijkl}, (D1)$$

where coefficients c_i , c_j , c_k , c_l represent directional cosines along the i, j, k, l axes. In the transformation from the HTT

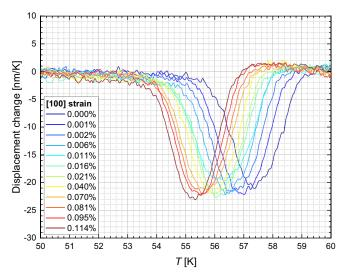


FIG. 11. The anomaly in displacement change $(\Delta L/\Delta T)$ of the strain cell measured in cooling $(r=1~{\rm K/min})$ for different applied stresses along the [100] direction. The anomaly temperature coincides with the structural transition temperature $T_{\rm LTT}=57.5~{\rm K}$ at zero applied stress. For increased strain values shown in the legend, the anomaly shifts to a lower temperature of 55.5 K.

to the LTT crystallographic axes, we can limit ourselves to the rotation about the z axis ($\theta = \pm 45^{\circ}$). Equation (D1) can then be condensed into a 6×6 rotation matrix:

$$\mathbf{R} = \begin{pmatrix} c^2 & s^2 & 0 & 0 & 0 & 2cs \\ s^2 & c^2 & 0 & 0 & 0 & -2cs \\ 0 & 0 & 1 & 0 & 0 & 0 \\ 0 & 0 & 0 & c & s & 0 \\ 0 & 0 & 0 & -s & c & 0 \\ -cs & cs & 0 & 0 & 0 & c^2 - s^2 \end{pmatrix}, \quad c \equiv \cos \theta \\ s \equiv \sin \theta,$$
(D2)

which acts on a stiffness tensor $\mathbf{C}^{(LTT)} = \mathbf{R}\mathbf{C}^{(HTT)}\mathbf{R}^T$. Finally, to make the expressions more convenient to analyze and use, we replace the stiffness constant by utilizing the relation

$$\begin{pmatrix}
\mathbf{C}^{(\text{HTT,LTT})}
\end{pmatrix}^{-1} = \mathbf{S}^{(\text{HTT,LTT})} \\
= \begin{pmatrix}
\frac{1}{Y_{[100]}} & -\frac{\nu_{\text{in}}}{Y_{[100]}} & -\frac{\nu_{\text{out}}}{Y_{[100]}} & 0 & 0 & 0 \\
-\frac{\nu_{\text{in}}}{Y_{[100]}} & \frac{1}{Y_{[100]}} & -\frac{\nu_{\text{out}}}{Y_{[100]}} & 0 & 0 & 0 \\
-\frac{\nu_{\text{out}}}{Y_{[100]}} & -\frac{\nu_{\text{out}}}{Y_{[100]}} & \frac{1}{I_{0}} & 0 & 0 & 0 \\
0 & 0 & 0 & \frac{1}{G_{zx}} & 0 & 0 \\
0 & 0 & 0 & 0 & \frac{1}{G_{zx}} & 0 \\
0 & 0 & 0 & 0 & 0 & \frac{1}{G_{yy}}
\end{pmatrix}, (D3)$$

where the elastic compliance matrix **S** is given in terms of Young and shear moduli ($Y_{[100]} = 233 \,\text{GPa}$, $Y_{[001]} = 176 \,\text{GPa}$, $G_{zx} \approx G_{xy} = 66.4 \,\text{GPa}$) and Poisson ratios ($v_{\text{in}} = 0.18$, $v_{\text{out}} = 0.27$). In this work, we use elastic stiffness constants given for the LTT phase when setting up the model, but then we express the results using the elastic parameters of the HTT lattice. The reason for this is twofold: the sample is oriented and glued into the strain cell with respect to the HTT axes, and we can readily use the elastic data from other sources to gauge the induced strain and expected $T_{\text{CO,SO}}$ suppression.

To accentuate the role of the symmetry-breaking stress on the transition, we use (anti)symmetrized strain components $\varepsilon_{A_{1g,1}} = \frac{1}{2}(\varepsilon_{xx} + \varepsilon_{yy})$, $\varepsilon_{A_{1g,2}} = \varepsilon_{zz}$, and $\varepsilon_{B_{1g}} = \frac{1}{2}(\varepsilon_{xx} - \varepsilon_{yy})$, $\varepsilon_{B_{2g}} = \varepsilon_{xy}$. From here, we construct a model taking into account five contributions to free the energy:

$$F = F_{\Psi} + F_{\Psi\varepsilon} + F_{\Psi\Phi} + F_{\varepsilon} + F_{\sigma},$$

$$F_{\Psi} = \Psi_{B_{2g}}^{2} a (T - T_{SO}) + \Psi_{B_{2g}}^{4} b / 2,$$

$$F_{\Psi\varepsilon} = \alpha_{1} \varepsilon_{A_{1g,1}} \Psi_{B_{2g}}^{2} + \alpha_{2} \varepsilon_{A_{1g,2}} \Psi_{B_{2g}}^{2} + \beta \varepsilon_{B_{1g}}^{2} \Psi_{B_{2g}}^{2} + \gamma \varepsilon_{B_{2g}} \Psi_{B_{2g}},$$

$$+ \gamma \varepsilon_{B_{2g}} \Psi_{B_{2g}},$$

$$F_{\Psi\Phi}^{(CO,SO)} = \delta \Phi_{B_{2g}}^{2} \Psi_{B_{2g}}^{2},$$

$$F_{\varepsilon} = \varepsilon_{A_{1g,1}}^{2} (C_{11} + C_{12}) + C_{33} \varepsilon_{A_{1g,2}}^{2} / 2 + \varepsilon_{B_{1g}}^{2} (C_{11} - C_{12}) + 2C_{13} \varepsilon_{A_{1g,1}} \varepsilon_{A_{1g,2}} + 2C_{66} \varepsilon_{B_{2g}}^{2},$$

$$F_{\sigma} = -\sigma \cdot \varepsilon,$$
(D4)

where $\Psi^2_{B_{2g}}$ represents an emergent spin order that transforms as a B_{2g} irreducible representation of a D_{4h} point group, and $\Phi_{B_{2g}}$ is a structural order parameter taken to be temperature-independent for reasons listed in the article. All the contributions contain the lowest-order terms in order parameters, with coupling constants expressed as α_1 , α_2 ,

 β , γ , and δ . a and b (a,b>0) are the standard Landau expansion parameters. The last, elastic energy contribution, sets the strains as a function of the applied uniaxial stress. At the minimum of the total free energy in the absence of the spin/structural order, F_{σ} must be exactly equal to the quadratic form in strains F_{ε} .

We can find the equilibrium strain as a solution to the set of minimization conditions $\frac{\partial F}{\partial \varepsilon_i} = 0$ given for all the symmetric and antisymmetric combinations of the strain. Evaluating the solution at $\sigma_{[100]} = 0$ GPa or $\sigma_{[110]} = 0$ GPa implies the emergence of spontaneous strains when the system enters an ordered phase:

$$\varepsilon_{A_{1g;1}} = \frac{\Psi_{B_{2g}}^{2}[(\nu_{\text{in}} - 1)\alpha_{1} + 2\nu_{\text{out}}\alpha_{2}]}{2Y_{[100]}},$$

$$\varepsilon_{A_{1g;2}} = \frac{\Psi_{B_{2g}}^{2}(-Y_{[100]}\alpha_{2} + Y_{[001]}\nu_{\text{out}}\alpha_{1})}{Y_{[100]}Y_{[001]}},$$

$$\varepsilon_{B_{2g}} = -\frac{\Psi_{B_{2g}}\gamma(\nu_{\text{in}} + 1)}{8Y_{[100]}},$$

$$\varepsilon_{B_{1g}} = \varepsilon_{E_{g}(1)} = \varepsilon_{E_{g}(2)} = 0.$$
(D5)

Introduction of the equilibrium strain into the free-energy model and minimization with respect to the order parameter $\Psi_{B_{2g}}$ results in a third-order polynomial in $\Psi_{B_{2g}}$, with a single real solution. One may argue that the complex solutions to the order parameters are standard; however, we must disregard them as we have taken $\Psi_{B_{2g}}$ as the order magnitude, and we have allowed for a linear coupling in $\Psi_{B_{2g}}$. Therefore, such a solution would yield a nonphysical complex free energy.

The real solution for the stress $\sigma_{[100]}$ applied along the [100] axis implies that the $T_{CO,SO}$ is suppressed in a linear fashion:

$$\frac{\partial T_{\text{CO,SO}}}{\partial \sigma_{[100]}} = \frac{(1 - \nu_{\text{in}})\alpha_1}{2Y_{[100]}a} - \frac{\nu_{\text{out}}\alpha_2}{Y_{[100]}a} \equiv f(\alpha_1, \alpha_2).$$
 (D6)

Here, we observe that coupling constants β and γ are absent; thus, only the induced symmetric strains govern the suppression. We will encounter this expression multiple times, and therefore we define it as a function $f(\alpha_1, \alpha_2)$. We purposefully consider $Y_{[100]}$ as a constant in $f(\alpha_1, \alpha_2)$ since the following expressions can always be expressed using exactly $Y_{[100]}$, irrespective of the direction of the applied stress. As noted in the article, we do not observe a measurable change in either T_{SO} or T_{CO} with this sample orientation, so that we can approximate $f(\alpha_1, \alpha_2) \approx 0 \text{ K/GPa}$. When the stress $\sigma_{[110]}$ is applied to the sample, both T_{SO} and T_{CO} suppression rates are quadratic in $\sigma_{[110]}$. The linear term has the exact form as with the $\sigma_{[100]}$ stress, while the quadratic part depends on the sample's shear modulus G_{xy} :

$$\Delta T_{\text{CO,SO}}(\sigma_{[110]}) = f(\alpha_1, \alpha_2) \sigma_{[110]} - \frac{4\beta}{G_{xy}^2 a} \sigma_{[110]}^2$$

$$\approx -\frac{4\beta}{G_{xy}^2 a} \sigma_{[110]}^2. \tag{D7}$$

The $T_{\text{CO,SO}}$ suppression under the hydrostatic regime can also be expressed using $f(\alpha_1, \alpha_2)$, so we can reduce the

dependence to

$$\frac{\partial T_{\text{CO,SO}}}{\partial p} = f(\alpha_1, \alpha_2) - \frac{\nu_{\text{out}} \alpha_1}{Y_{[100]} a} + \frac{\alpha_2}{Y_{[001]} a}
\approx -\frac{\nu_{\text{out}} \alpha_1}{Y_{[100]} a} + \frac{\alpha_2}{Y_{[001]} a}.$$
(D8)

Note that the symmetric strain contribution $f(\alpha_1, \alpha_2)$ is present in both expressions for the $T_{\text{CO,SO}}$ suppression rate. However, as discussed earlier, it seems to be negligible.

Now, we turn our attention to the model extension, which describes the effect of the external magnetic field. The standard way of treating the in-plane external magnetic field is to include a Zeeman contribution $F_{\text{Zeeman}} = \mu \mathbf{H} \cdot \mathbf{m}(\Psi_{B_{2g}})$, where $\mathbf{m}(\Psi_{B_{2g}})$ represents a magnetic moment associated with the order parameter $\Psi_{B_{2g}}$. Unfortunately, it is immediately evident that such a contribution would lead to a change in T_{SO} at all strains. In our model, we propose a two-component order parameter by introducing in-plane order parameters which are defined by different symmetry properties: $\Psi_{B_{1g}}$ transforms as B_{1g} , and $\Psi_{B_{2g}}$ transforms as B_{2g} representation of the D_{4h} point group. We proceed to write down the Landau model in the absence of strain up to the fourth-order invariants:

$$F_{\Psi} = a(T - T_{SO}) \left(\Psi_{B_{1g}}^2 + \Psi_{B_{2g}}^2 \right) + \frac{b \left(\Psi_{B_{1g}}^4 + \Psi_{B_{2g}}^4 \right)}{2} + c \Psi_{B_{1g}}^2 \Psi_{B_{2g}}^2.$$

Here, we realize that the assumption $c \approx b$ allows for a convenient reparametrization of the order parameters:

$$\begin{pmatrix} \Psi_{B_{1g}} \\ \Psi_{B_{2g}} \end{pmatrix} = \begin{pmatrix} \Psi_0 \cos(\varphi) \\ \Psi_0 \sin(\varphi) \end{pmatrix}, \tag{D9}$$

where Ψ_0 represents a total order magnitude, and φ is an angle that defines the mixing of the two components. The minimization of the proposed Landau model with respect to Ψ_0 determines that the spin order $\Psi_0 = \sqrt{a(T-T_{\rm SO})/b}$ sets in strictly at $T_{\rm SO}$ irrespective of the component mixing angle

 φ . The crucial difference from the single-component model is that we must include all the strain-coupling to the lowest order of $\Psi_{B_{1e}}$ and $\Psi_{B_{1e}}$:

$$F_{\Psi_{B_{1g}}} = \alpha_{11} \varepsilon_{A_{1g;1}} \Psi_{B_{1g}}^2 + \alpha_{21} \varepsilon_{A_{1g;2}} \Psi_{B_{1g}}^2 + \beta_{21} \varepsilon_{B_{2e}}^2 \Psi_{B_{1e}}^2 + \beta_{11} \varepsilon_{B_{1g}} \Psi_{B_{1g}},$$
(D10)

$$\begin{split} F_{\Psi_{B_{2g}}} &= \alpha_{12} \varepsilon_{A_{1g;1}} \Psi_{B_{2g}}^2 + \alpha_{22} \varepsilon_{A_{1g;2}} \Psi_{B_{2g}}^2 \\ &+ \beta_{12} \varepsilon_{B_{1g}}^2 \Psi_{B_{2g}}^2 + \beta_{22} \varepsilon_{B_{2g}} \Psi_{B_{2g}}, \end{split} \tag{D11}$$

where coefficients α_{ij} define coupling strength to the symmetric strain, and β_{ij} to the asymmetric strain (we take the first index i to refer to the strain component, e.g., $i=1 \rightarrow \varepsilon_{A_{1g,1}}$, and the second index j to refer to the symmetry of the order parameter). The spin-structure coupling and the elastic energy contribution are left unchanged.

With the introduction of the order parameter reparametrization and the minimization of the free energy with respect to Ψ_0 , in the case of the $\sigma_{[110]}$ strain, we obtain

$$\Delta T_{SO}(\sigma_{[110]}, \varphi) = [f(\alpha_{11}, \alpha_{21}) \sin^2 \varphi + f(\alpha_{12}, \alpha_{22}) \cos^2 \varphi] \sigma_{110} - \frac{\beta_{12} \cos^2 (\varphi)}{G_{vv}^2 a} \sigma_{110}^2.$$
 (D12)

We have already demonstrated that the suppression rate $f(\alpha_{12},\alpha_{22})$, related to the $\Psi_{B_{2g}}$ spin order, vanishes, but one should not assume the same for the $f(\alpha_{11},\alpha_{21})$ rate. Nevertheless, by fitting the quadratic function to our measurements, we can show that the quadratic suppression constant $\beta_{\rm eff}$ is indeed reduced by some factor $\cos^2\varphi$. Finally, more experimental data are needed to get the exact dependence of the mixing angle φ on the orientation of the applied in-plane magnetic field. However, by looking at the crystal symmetry, we must assume that the model is symmetric to rotation by $\phi=90^\circ$ when the spin stripe direction coincides again with Cu-O bonds. To correlate the model to the structure, in the main article we use the reparametrization with $\varphi=2\varphi$.

K. Kumagai, K. Kawano, I. Watanabe, K. Nishiyama, and K. Nagamine, Hyperfine Interact. 86, 473 (1994).

^[2] T. Goto, S. Kazama, K. Miyagawa, and T. Fukase, J. Phys. Soc. Jpn. 63, 3494 (1994).

^[3] M. Hücker, M. v. Zimmermann, G. D. Gu, Z. J. Xu, J. S. Wen, G. Xu, H. J. Kang, A. Zheludev, and J. M. Tranquada, Phys. Rev. B 83, 104506 (2011).

^[4] Z. Guguchia, R. Khasanov, A. Shengelaya, E. Pomjakushina, S. J. L. Billinge, A. Amato, E. Morenzoni, and H. Keller, Phys. Rev. B 94, 214511 (2016).

^[5] M. Hücker, M. v. Zimmermann, M. Debessai, J. S. Schilling, J. M. Tranquada, and G. D. Gu, Phys. Rev. Lett. 104, 057004 (2010).

^[6] G. Fabbris, M. Hücker, G. D. Gu, J. M. Tranquada, and D. Haskel, Phys. Rev. B 88, 060507(R) (2013).

^[7] G. Fabbris, M. Hücker, G. D. Gu, J. M. Tranquada, and D. Haskel, High Press. Res. 36, 348 (2016).

^[8] M. K. Crawford, R. L. Harlow, S. Deemyad, V. Tissen, J. S. Schilling, E. M. McCarron, S. W. Tozer, D. E. Cox, N. Ichikawa, S. Uchida *et al.*, Phys. Rev. B 71, 104513 (2005).

^[9] B. Simovič, M. Nicklas, P. C. Hammel, M. Hücker, B. Büchner, and J. D. Thompson, Europhys. Lett. 66, 722 (2004).

^[10] T. J. Boyle, M. Walker, A. Ruiz, E. Schierle, Z. Zhao, F. Boschini, R. Sutarto, T. D. Boyko, W. Moore, N. Tamura *et al.*, Phys. Rev. Res. 3, L022004 (2021).

^[11] S. Arumugam, N. Môri, N. Takeshita, H. Takashima, T. Noda, H. Eisaki, and S. Uchida, Phys. Rev. Lett. 88, 247001 (2002).

^[12] N. Takeshita, T. Sasagawa, T. Sugioka, Y. Tokura, and H. Takagi, J. Phys. Soc. Jpn. 73, 1123 (2004).

^[13] G. Gu, M. Hücker, Y.-J. Kim, J. Tranquada, Q. Li, and A. Moodenbaugh, J. Cryst. Growth 287, 318 (2006).

^[14] J. M. Tranquada, G. D. Gu, M. Hücker, Q. Jie, H.-J. Kang, R. Klingeler, Q. Li, N. Tristan, J. S. Wen, G. Y. Xu *et al.*, Phys. Rev. B 78, 174529 (2008).

- [15] A. Narath, Phys. Rev. 162, 320 (1967).
- [16] D. E. MacLaughlin, J. D. Williamson, and J. Butterworth, Phys. Rev. B 4, 60 (1971).
- [17] D. C. Johnston, Phys. Rev. B 74, 184430 (2006).
- [18] P. M. Singer, A. W. Hunt, and T. Imai, Phys. Rev. Lett. 88, 047602 (2002).
- [19] D. Pelc, H.-J. Grafe, G. D. Gu, and M. Požek, Phys. Rev. B 95, 054508 (2017).
- [20] A. W. Hunt, P. M. Singer, A. F. Cederström, and T. Imai, Phys. Rev. B 64, 134525 (2001).
- [21] H.-J. Grafe, N. J. Curro, M. Hücker, and B. Büchner, Phys. Rev. Lett. 96, 017002 (2006).
- [22] P. M. Singer, A. W. Hunt, A. F. Cederström, and T. Imai, Phys. Rev. B 60, 15345 (1999).
- [23] N. J. Curro, P. C. Hammel, B. J. Suh, M. Hücker, B. Büchner, U. Ammerahl, and A. Revcolevschi, Phys. Rev. Lett. 85, 642 (2000).
- [24] D. Pelc, M. Vučković, H.-J. Grafe, S.-H. Baek, and M. Požek, Nat. Commun. 7, 12775 (2016).
- [25] C. W. Hicks, M. E. Barber, S. D. Edkins, D. O. Brodsky, and A. P. Mackenzie, Rev. Sci. Instrum. 85, 065003 (2014).
- [26] M. Nohara, T. Suzuki, Y. Maeno, T. Fujita, I. Tanaka, and H. Kojima, Phys. Rev. B 52, 570 (1995).
- [27] B. J. Suh, P. C. Hammel, M. Hücker, B. Büchner, U. Ammerahl, and A. Revcolevschi, Phys. Rev. B 61, R9265 (2000).
- [28] S.-H. Baek, Y. Utz, M. Hücker, G. D. Gu, B. Büchner, and H.-J. Grafe, Phys. Rev. B **92**, 155144 (2015).
- [29] N. Bloembergen, E. M. Purcell, and R. V. Pound, Phys. Rev. 73, 679 (1948).
- [30] A. P. Dioguardi, N. apRoberts Warren, A. C. Shockley, S. L. Bud'ko, N. Ni, P. C. Canfield, and N. J. Curro, Phys. Rev. B 82, 140411(R) (2010).
- [31] F. L. Ning, M. Fu, D. A. Torchetti, T. Imai, A. S. Sefat, P. Cheng, B. Shen, and H.-H. Wen, Phys. Rev. B 89, 214511 (2014).
- [32] Z. Guguchia, D. Das, C. N. Wang, T. Adachi, N. Kitajima, M. Elender, F. Brückner, S. Ghosh, V. Grinenko, T. Shiroka *et al.*, Phys. Rev. Lett. 125, 097005 (2020).
- [33] W. Schottenhamel, Ph.D. thesis, Technische Universität Dresden, 2016.

- [34] M. K. Crawford, R. L. Harlow, E. M. McCarron, W. E. Farneth, J. D. Axe, H. Chou, and Q. Huang, Phys. Rev. B 44, 7749 (1991).
- [35] J. D. Axe and M. K. Crawford, J. Low Temp. Phys. 95, 271 (1994).
- [36] J. Fink, V. Soltwisch, J. Geck, E. Schierle, E. Weschke, and B. Büchner, Phys. Rev. B 83, 092503 (2011).
- [37] M. Hücker, G. D. Gu, and J. M. Tranquada, Phys. Rev. B 78, 214507 (2008).
- [38] N. Plakida and V. Shakhmatov, Physica C 153-155, 233 (1988).
- [39] Y. Ishibashi, J. Phys. Soc. Jpn. **59**, 800 (1990).
- [40] A. Migliori, W. M. Visscher, S. Wong, S. E. Brown, I. Tanaka, H. Kojima, and P. B. Allen, Phys. Rev. Lett. 64, 2458 (1990).
- [41] M. Hücker, V. Kataev, J. Pommer, U. Ammerahl, A. Revcolevschi, J. M. Tranquada, and B. Büchner, Phys. Rev. B 70, 214515 (2004).
- [42] B. Keimer, R. J. Birgeneau, A. Cassanho, Y. Endoh, M. Greven, M. A. Kastner, and G. Shirane, Z. Phys. B 91, 373 (1993).
- [43] A. Togo, F. Oba, and I. Tanaka, Phys. Rev. B 78, 134106 (2008).
- [44] X. Lu, K.-F. Tseng, T. Keller, W. Zhang, D. Hu, Y. Song, H. Man, J. T. Park, H. Luo, S. Li et al., Phys. Rev. B 93, 134519 (2016).
- [45] J.-H. Chu, H.-H. Kuo, J. G. Analytis, and I. R. Fisher, Science 337, 710 (2012).
- [46] M. S. Ikeda, T. Worasaran, J. C. Palmstrom, J. A. W. Straquadine, P. Walmsley, and I. R. Fisher, Phys. Rev. B 98, 245133 (2018).
- [47] N. Plakida, *High-Temperature Cuprate Superconductors: Experiment, Theory, and Applications*, Springer Series in Solid-State Sciences (Springer, Berlin, 2010).
- [48] Z. Guguchia, D. Das, G. Simutis, T. Adachi, J. Küspert, N. Kitajima, M. Elender, V. Grinenko, O. Ivashko, M. V. Zimmermann et al., arXiv:2302.07015v1.
- [49] T. Hashimoto and A. Ikushima, Rev. Sci. Instrum. 51, 378 (1980).
- [50] P. M. Singer, A. Arsenault, T. Imai, and M. Fujita, Phys. Rev. B 101, 174508 (2020).
- [51] V. F. Mitrović, M.-H. Julien, C. de Vaulx, M. Horvatić, C. Berthier, T. Suzuki, and K. Yamada, Phys. Rev. B 78, 014504 (2008).